DTM-Padé Numerical Simulation of Electrohydrodynamic Ion Drag Medical Pumps with Electrical Hartmann and Electrical Reynolds Number Effects

O. Anwar Bég[1,*], M.M. Rashidi[2], M.T. Rastegari[3], Tasveer A. Bég[4], S.S. Motsa[5] and Amna Halim[6]

[1]*GORT Engovation – Propulsion and Biomechanics, Southmere Ave., Bradford, BD73NU, England, UK*

[2]*Mechanical Engineering Department, University of Michigan-Shanghai, Shanghai, China*

[3]*Mechanical Engineering Department, Engineering Faculty of Bu-Ali Sina University, Hamedan, Iran*

[4]*Engineering Mechanics Research, Albert Road, Levenshulme, Manchester, M192AB, England, UK*

[5]*School of Mathematics, Statistics and Computer Science, University of KwaZulu-Natal, Private Bag X01, Scottsville 3209, Pietermaritzburg, South Africa*

[6]*Polymathematics, Braystan Gardens, Gatley, Cheadle, Stockport, SK84NU, Manchester, England, UK*

Abstract: The DTM-Padé method, a combination of the differential transform method (**DTM**) and Padé approximants, is applied to provide highly accurate, stable and fast semi-numerical solutions for several nonlinear flow regimes of interest in electrohydrodynamic ion drag pumps, arising in chemical engineering processing. In both regimes studied, the transformed, dimensionless ordinary differential equations subject to realistic boundary conditions are solved with DTM-Padé and excellent correlation with numerical quadrature is achieved. The influence of electrical Reynolds number (Re_E), electrical slip number (E_{sl}), electrical source number (E_s) and also electrical Hartmann number (Ha_e) are examined graphically. Applications of this study include novel ion drag pumps and astronautical micro-reactors. This study constitutes the first application of the DTM-Padé semi-computational algorithm to electrohydrodynamic biotechnology flows.Furthermore the range of solutions given significantly extends the existing computations in previous studies and provides a much more general analysis of ion drag pump electrohydrodynamics, of direct relevance to medical drug delivery systems.

Keywords: Electrohydrodynamics, Semi-numerical solutions, Differential Transform Method (DTM), Padé approximants, numerical shooting quadrature, electrical Hartmann number, ion drag pumps, medical drug delivery.

1. INTRODUCTION

In recent years considerable development has taken place in the study of electrofluid systems. Electrohydrodynamics (**EHD**) exploits the use of electrical fields to control transport phenomena in flowing fluids. Many biomedical and biotechnology applications of such flows exist including electrostatic precipitators [1], colloidal particle orientation with alternating or direct current electric field applied normal to an interface [2], dielectric pump design [3], co-planar microelectrode design [4], regulation of nickel particle granular hopper flows in medical (pharmaceutical) powder processing [5] and ion flow in divertor tokamak reactors [6]. Further recent applications of EHD flows which may exploit transverse or radial electrical fields include combustion control [7], smart electro-rheological fluids [8], electro-spray liquid atomization using Taylor cone electrohydrodynamic jets [9], protein biomolecule separation with pulsed electrofluid dynamics [10], EHD printing technology [11], astronautical vehicle surface modification with electro-hydroynamic sprays [12] and boundary layer control in ionized hypersonic flows [13]. Numerical simulations of EHD flows have in particular been a major area of investigation, since the nature of mathematical models describing EHD is strongly nonlinear and coupled and necessitates numerical solutions. Bég *et al.* [14] studied the transport in EHD ion drag pumping using the computational network simulation method (NSM). Mastroberardino [15] analyzed nonlinear axisymmetric electrohydrodynamic using the homotopy analysis method (HAM). Chen *et al*. [16] studied EHD flow in a round pipe using a PISO (pressure-implicit with splitting of operators) numerical scheme under a periodic boundary condition, showing that a vortex ring is generated between the electrodes due to the nonuniform distribution of velocity and charge density during the starting process, and that spatial distribution of the pressure is similar to that of the electric potential between the electrodes. Fengt and Scott [17] examined numerically the axisymmetric steady flows driven by an electric field about a deformable fluid drop suspended

*Address correspondence to this author at the GORT Engovation – Propulsion and Biomechanics, Southmere Ave., Bradford, BD73NU, England, UK; Tel: +44 01274 504 600; Fax: +44 01274 504 601;
E-mail: gortoab@gmail.com

E-ISSN: 2311-1755/13

in an immiscible fluid with the leaky dielectric model and a Galerkin finite-element method with an elliptic mesh generation scheme. They showed that under conditions of creeping flow and vanishingly small drop deformations, the results of finite-element computations recover the asymptotic results. Vázquez *et al.* [18] used a particle-in-cell and the finite element-flux corrected transport method to simulate injection instabilities in the development of electro-convection between two parallel plates. They considered unipolar injection (both strong and weak injections) between two plane electrodes immersed in a dielectric liquid and showed that simulations are problematic for small oscillations of the velocity and electric current. Xuan and Zhang [19] used a least-squares meshfree method (LSMFM) based on the first-order velocity–pressure–vorticity formulation for the Stokes flow, electric potential–electric field strength expression for electric field and temperature–heat flux equations for heat transfer to investigate computationally the two-dimensional electrothermally-induced fluid flow over microelectrodes. Verplaetsen and Berghmans [20] studied numerically the effect of electric field on the liquid-vapor interface during film boiling from a horizontal surface of stagnant fluids (pool boiling) using a fourth-order Runge-Kutta integration technique to calculate the shape of the interface and a boundary element method (BEM) to evaluate the electric field. Further studies of EHD transport have utilized the hybrid boundary element method - method of characteristics (BEM-MOC) approach [21], Lattice-Boltzmann method (LBM) [22], a ghost fluid method (GFM) with direct numerical simulation (DNS) [23], a finite difference method (FDM) [24] and the semi-numerical homotopy perturbation method (HPM) [25].

Another powerful semi-numerical-analytic-technique which as been implemented in multi-physical fluid mechanics is the Differential Transform Method (DTM) introduced originally by Zhou [26] for electrical circuit theory analysis of linear and non-linear initial value problems. DTM formalizes the Taylor series in a totally different manner and differs from the customary higher order Taylor series method, the latter requiring symbolic computation a feature which unfortunately increases considerably the computational expense for large orders. DTM obtains a polynomial series solution by means of an *iterative* procedure. The DTM is therefore a robust, alternative procedure for obtaining analytic Taylor series solution of linear or nonlinear differential equations. With this method, it is possible to obtain highly accurate results or exact solutions for differential equations. DTM circumvents the need for linearization or perturbations and excessive computational work and round-off errors can be avoided. DTM implements specific transformation rules to transform original functions, including boundary conditions, into a set of algebraic functions. Solving the algebraic set by iteration, the results generated demonstrate very high accuracy. DTM has been employed in numerous diverse topics in fluid dynamics in recent years. These include hydromagnetic flows [27], mixed convection flows [28], magneto-micropolar flows [29], biomagnetic flows [30], swirling plasma flows [31], nuclear propulsion [32], non-Newtonian flows [33], combustion and fire dynamics [34], extra-corporeal surgical magnetic field flow control [35], reactive flows [36], multi-phase biophysical transport [37] and hypersonic aerodynamics [38]. This diverse spectrum of successful applications has strongly verified the validity, effectiveness and flexibility of DTM, which has in many of these studies been combined with Padé approximants to *satisfy infinity boundary conditions*. **DTM-Padé** simulation has emerged as a powerful semi-numerical tool and the present article focuses on employing this approach to simulate *electrohydrodynamic* flows for the first time. We study in detail *two nonlinear boundary value problems* in electrohydrodynamic ion drag pump systems, and thereby re-examine earlier studies by McKee *et al.* [39] and Seyed-Yagoobi *et al.* [40]. Extensive details of DTM solutions are provided and benchmarked also with numerical shooting quadrature solutions. The high accuracy and potential of DTM in electrohydrodynamic flows is demonstrated. The current study finds important applications in medical electronics [41] and also cryogenic systems in bio-astronautics [42]. In the present study we extend the range of electrohydrodynamic parameters examined in previous studies to provide a more general analysis of ion drag transport in biotechnology. Electrical Reynolds number, electrical source number, electrical slip number and electrical Hartmann number are all addressed in much more detail than in previous investigations. This therefore allows bioengineers and biotechnologists a better perspective of potential operating abilities of EHD pumps in medical drug delivery.

2. MATHEMATICAL MODELS

Case 1: Electrohydrodynamic Ion Drag Flow in a Circular Cylindrical Conduit

McKee *et al.* [39] originally studied this regime. It was later examined by Mastroberardino [15] using the homotopy analysis method (HAM) and alternative

solutions were given by Khan *et al*. [25] using the homotopy perturbation method (HPM), a special case of HAM. It has also been simulated very recently using a Chebyschev spectral collocation algorithm by Bég *et al.* [43]. Thusfar however it has not been analyzed with the DTM approach or any of its variants and is therefore an excellent test case for this method in electrohydrodynamic studies. Prior to developing **DTM-Padé** semi-numerical solutions, we summarize the fundamentals of the problem. Consider an electrical field $\vec{E}_0$, generated by a voltage *V*, across the length of a conduit (Figure **1**), in a axisymmetric coordinate system (*r,z*) where *r* is radial coordinate and *z* is axial coordinate. Assuming only a single type of ionized particle is present in the dielectric fluid medium; the current density $\vec{J}$ is then influenced by the ion mobility (*K*) of the particles:

$$\vec{J} = \rho_f [K\vec{E}_0 + \vec{v}] \tag{1}$$

in which ρ_f denotes the free charge density of the ion/fluid medium. For *fully developed flow*, McKee *et al.* [39] reduce the generalized vectors for velocity, current density and free charge density to the following form:

$$\vec{v} = (0,0,w(r)),\ \ \vec{j} = (0,0,j(r)),\ \ \rho_f = \rho(r) \tag{2}$$

with the axial pressure gradient, $\frac{\partial p}{\partial z}$ assumed constant. It follows that the Navier-Stokes equations for the regime reduce to the following equation, in which the fluid velocity depends nonlinearly on the electrical field acting across it:

$$\frac{\partial p}{\partial z} = \rho_f E_0 + \frac{\mu}{r}\frac{d}{dr}\left[r\frac{dw}{dr}\right] \tag{3}$$

where p is pressure, μ is the dynamic viscosity of the dielectric fluid, E_o is electrical field ($|E_0| = V/L$). Two different *time scales* exist, for a typical velocity scale, *U* and length, *L*, which control the coupling between the fluid and the ions, which take the forms:

$$t_c = \frac{\varepsilon_0}{K\rho_0}, \qquad t_f = \frac{L}{U} \tag{4}$$

The first of these times is the charge relaxation time for the ions (particles), t_c, in which ε_0 is the constant permittivity of free space (Farads/m), ρ_0 is the charge density at the inlet screen (emitter). The second time scale is the fluid transport time, t_f. The electrical Reynolds number is obtained from the ratio of these two time scales, and embodies the *ratio of inertial force to electrical force*. It can be used to represent the efficiency of energy conversion in EHD ion drag pumps. Fluid convection determines the free charge density of the ion/fluid medium at *high* electrical Reynolds numbers (ρ_f). Assuming that the current density is uniform over the cross-section at the pump conduit inlet, i.e. $j\ (z=0) = j_0$, then the charge density from eqn. (1) becomes $\rho_f(r) = \frac{j_0}{KE_0 + w(r)}$. With these simplifications, we arrive at the following equation for the *fully developed axial flow velocity*, *w(r)*, as originally derived by McKee *et al.* [39]:

$$\frac{\partial p}{\partial z} = \frac{j_0 E_0}{KE_0 + w} + \frac{\mu}{r}\frac{d}{dr}\left[r\frac{dw}{dr}\right] \tag{5}$$

The appropriate boundary conditions are specified by taking the velocity gradient and velocity as vanishing at the conduit centre and wall, respectively, viz:

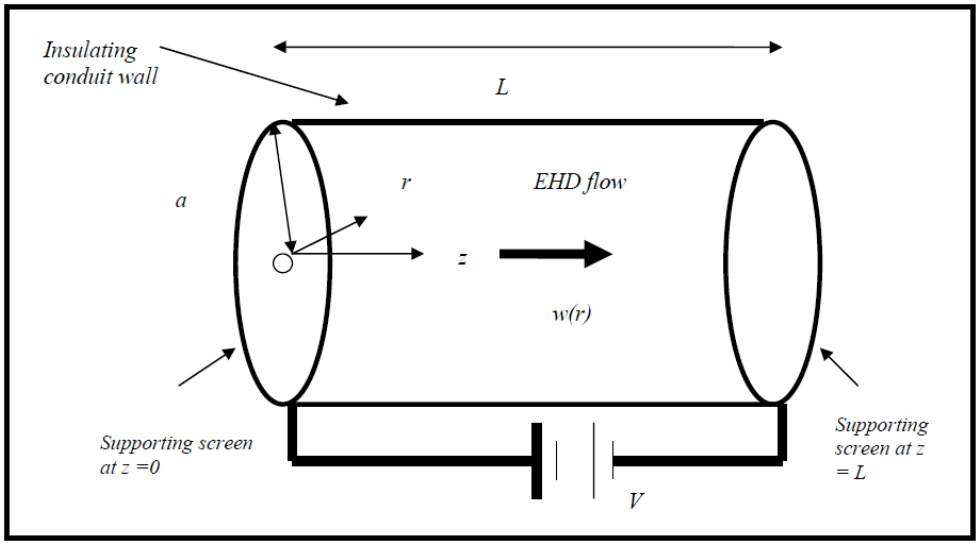

Figure 1: *Case 1* - Physical model.

$$\frac{dw}{dr} = 0 \ at \ r = 0; \ w = 0 \ at \ r = a \tag{6}$$

w is bounded and symmetric about r = 0. Non-dimensionalizing eqn. (5) using the transformed variables, $r^* = r / a$ and $w^* = -(w / KE_0\alpha)$, we obtain:

$$\frac{d^2w^*}{dr^{*2}} + \frac{1}{r^*}\frac{dw^*}{dr^*} + Ha^2{}_e\left[1 - \frac{w^*}{1-\alpha w^*}\right] = 0 \tag{7}$$

where $\alpha = \frac{K}{j_0}\frac{\partial p}{\partial z} - 1$ measures the *non-linearity* in eqn. (8) and $Ha_e = \sqrt{\frac{j_0 a^2}{\mu K^2 E_0}}$ is the *electric Hartmann number*, signifying the *ratio of electrical (Coulomb) to viscous forces* in the regime. The dimensionless boundary conditions (7) become:

$$\frac{dw^*}{dr^*} = 0 \ at \ r^* = 0; \ w^* = 0 \ at \ r^* = 1 \tag{8}$$

The EHD flow domain characterized by eqn. (8) has an electric Hartmann layer, which is analogous to the magnetic Hartmann layer and an electric Hartmann number Ha_e is invoked. At high Ha_e ions in the main flow regime will be subjected to weaker forces than those near the conduit wall. This electrical Hartmann layer will be diminished as electrical Hartmann number increases. Equation (7) under boundary conditions (8) constitute a *well-posed nonlinear two-point boundary value problem* which is solved using the **DTM** numerical approach, in due course.

Case 2: Unipolar DC EHD Pump Flow

In this second scenario, which has been considered in [40] was re-examined by Bég *et al.* [14] using a numerical tool known as the network simulation method (**NSM**) based on an electric circuit solver, **PSPICE**. This model has also been studied very recently by Bég *et al.* [43] with the Chebyschev spectral collocation computational technique. The flow model however deviates considerably from that in **Case 1**. The geometry of the problem is depicted in Figure **2**. In this case, we neglect electro-strictive forces and assume, following [40], that electrical field distribution is *uni-directional* and parallel to the flow direction with unipolar ions present in the fluid and constant mobility. The emitter and collector electrodes exert no effect on the fluid flow. Ion current and field distributions are also not influenced by surface charges on the insulating boundaries of the conduit. *Ion velocity* relative to *fluid velocity* is of the same order of magnitude as the fluid velocity to the electrodes. High ion density therefore exists in the medium, and this regime is very relevant to astronautical applications [42]. The conservation laws for electrical field, current density and electrical potential take the form:

Gauss's Law:

$$\nabla \cdot \varepsilon \vec{E} = \rho \tag{9}$$

Conservation of Charge:

$$\nabla \cdot \vec{J} + \frac{\partial \rho}{\partial t} = 0 \tag{10}$$

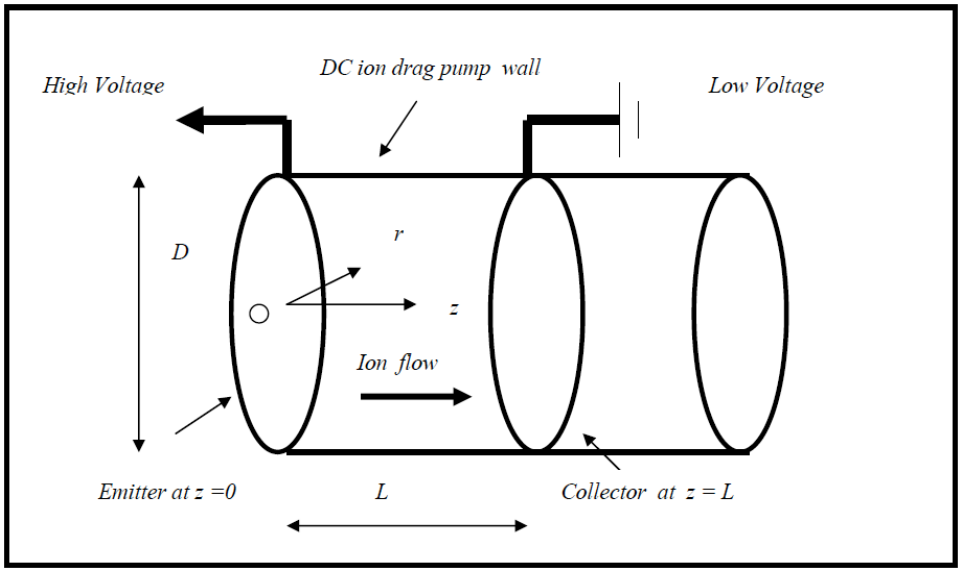

Figure 2: *Case 2: Physical* model.

Conservation of Electric Potential:

$$\vec{E} = -\nabla\Phi \tag{11}$$

When all three mechanisms of the current flow are combined we obtain the following relation for *total current density*:

$$\vec{J} = \sigma\vec{E} + \rho\vec{u} + \rho\mu\vec{E} \tag{12}$$

where ∇ is the gradient operator, $\vec{E}$ is electrical field vector (V/m^2), $\vec{J}$ is the current density vector (Amps/m^2), ρ is charge density (Coulomb/m^3), *t* is time, ε is permittivity (Faradays/m), Φ is potential (V), σ is electrical conductivity (S/m), $\vec{u}$ is fluid bulk velocity vector (m/s) and μ is ion mobility (m^2/Vs). Herein we shall study the situation where the electrical field located at emitter (i.e. at *z = 0* in Figure **2**), is *zero*. This is known as the *maximum pressure scenario* and has also been considered recently by Bég *et al.* [24]. In this study we further extend the computations presented in [24]. In equation (12), $\sigma\vec{E}$ is the *electrical conduction* term, $\rho\vec{u}$ is the *electrical convection* term and $\rho\mu\vec{E}$ is the *ionic mobility* term. The conservation equations (1) to (4) can be shown to reduce for constant property electrohydrodynamic flow to the following group of coupled, nonlinear, ordinary differential equations, in which *z* i.e. axial coordinate along the axis of the dc pump, is the only independent variable:

$$(\mu E + u)\frac{d\rho}{dz} + \frac{\sigma}{\varepsilon}\rho + \frac{\mu}{\varepsilon}\rho^2 = 0 \tag{13}$$

$$\frac{dE}{dz} - \frac{\rho}{\varepsilon} = 0 \tag{14}$$

$$E + \frac{d\Phi}{dz} = 0 \tag{15}$$

The relevant boundary conditions are:

$$z = 0\,(emitter): \quad E = 0;\ \rho = \rho_o;\ \Phi = V_o \tag{16}$$

Another important case, namely the *Operating Condition Scenario* can also be studied wherein electrical potential (Φ*) at the *collector* (*z= L*) is instead specified, rather than at the emitter. Normalization of the eqns. (13) to (15) is achieved with the following dimensionless variables [24]:

$$E^* = E\frac{L}{V_o}, \qquad \rho^* = \frac{\rho}{\rho_o}, \qquad \Phi^* = \frac{\Phi}{V_0},\ z^* = \frac{z}{L},$$

$$\mathrm{Re}_E = \frac{\varepsilon u}{\sigma L},\ E_{sl} = \frac{\frac{\mu V_0}{L}}{u},\ E_s = \frac{\rho_0 L^2}{\varepsilon V_0} \tag{17}$$

The non-dimensional conservation equations for electrical field (*E**), potential (Φ^*), and charge density (ρ^*), thereby reduce to:

$$(1 + E_{sl}E^*)\frac{d\rho^*}{dz^*} + \frac{\rho^*}{\mathrm{Re}_E} + E_s E_{sl}\rho^{*2} = 0 \tag{18}$$

$$\frac{dE^*}{dz^*} - E_s\rho^* = 0 \tag{19}$$

$$E^* + \frac{d\Phi^*}{dz^*} = 0 \tag{20}$$

The corresponding transformed boundary conditions are:

$$At\ z^* = 0\,(emitter): \quad E^* = 0;\ \rho^* = 1;\ \Phi^* = 1 \tag{21}$$

In the eqns. (18) to (20), Re_E is the electrical Reynolds number (symbolizing the relative significance of the charge convection effect and defined as the ratio of the timescales of charge convection by flow to that for charge relaxation by ohmic conduction), E_{sl} is the electrical slip number (which provides an estimate of the relative motion of the injected charges with regard to the bulk fluid velocity, *u*) and E_s is electrical source number (based on the analogy between the *Fourier thermal conduction* equation and *Poisson's electrostatics* equation). For engineering applications, it is pertinent to study the pressure generation (ΔP) and power efficiency (η_{EHD}). These are defined respectively, ignoring shear stresses along the conduit walls, as follows [24]:

$$\Delta P = \frac{1}{2}\varepsilon E_L^{\ 2} \tag{22}$$

$$\eta_{EHD} = \frac{power\ \ output}{power\ \ input} = \frac{(uA)\Delta P}{[V_0 - V_L]I} \tag{23}$$

where ΔP denotes pressure generation of the pump (N/m^2), E_L is the electrical field at the collector electrode (V/m), E_0 is the electrical field at the emitter electrode, *A* is the cross-sectional area of the unipolar dc EHD pump (m^2), V_0 is the voltage applied to the emitter electrode (V), V_L is the voltage applied to the collector electrode (V), *I* is current (Amps), *L* is distance between the electrode pair (m). As the electrical field becomes zero at the emitter electrode, the electrical current is therefore:

$$I = JA = \rho_0 uA \tag{24}$$

where ρ_0 is the charge density at the emitter electrode (Colulomb/m^3). It follows that the EHD efficiency is:

$$\eta = \frac{\frac{1}{2}\varepsilon E_L^{\,2}}{[V_0 - V_L]\rho_0} \tag{25}$$

In dimensionless form we have:

$$\eta = \frac{\frac{1}{2}E^*_L{}^2}{Es[1-\Phi^*_L]} \tag{26}$$

where E^*_L is the dimensionless electrical field at the collector electrode and Φ^*_L is the dimensionless potential at the collector electrode. The expression (26) associates η_{EHD}, directly with the electrical field values at the emitter and the collector electrodes. The coupled boundary value problem defined by eqns. (18) to (20) under conditions (21) is also solved subsequently by the **DTM** approach.

3. DIFFERENTIAL TRANSFORM METHOD (DTM)

DTM has a number of complex aspects associated with it. Here we present a summary of the pertinent steps involved in using this technique and then elaborate on the implementation of Padé approximants which accelerate convergence of the procedure. Further details of DTM-Padé simulation are available in Bég *et al.* [44] wherein it has been applied to micropolar non-Newtonian flows. The transformation of the k^{th} derivative of a function in one variable is as follows:

$$U(k) = \frac{1}{k!}\left[\frac{d^k u(k)}{dx^k}\right]_{z^*=z^*_0}, \tag{27}$$

In Eq. (27) $f(z^*)$ is the original function and $F(k)$ is transformed function, termed the *T-function* (it is also called the spectrum of $f(z^*)$ at $z^* = z^*_0$ in the K domain). The differential inverse transformation of $F(k)$ is defined as follows:

$$f(z^*) = \sum_{k=0}^{\infty} F(k)(z^* - z^*_0)^k. \tag{28}$$

Eq. (28) implies that the concept of the differential transform is derived from Taylor's series expansion; however this method does not evaluate the derivatives *symbolically*. Nevertheless relative derivatives are calculated by an iterative procedure that is described by the transformed equations of the original functions. In real applications, the function $f(z^*)$ in Eq. (28) is expressed by a *finite series* and can be written as:

Table 1: The Fundamental Operations of DTM

Original function	Transformed function
$w(x) = u(x) \pm v(x)$	$W(k) = U(k) \pm V(k)$
$w(x) = \lambda\, u(x)$	$W(k) = \lambda U(k), \lambda$ is a constant
$w(x) = x^r$	$W(k) = \delta(k-1)$, where $\delta(k-1) = \begin{cases} 1, & \text{if } k = r \\ 0, & \text{if } k \neq r \end{cases}$
$w(x) = \frac{du(x)}{dx}$	$W(k) = (k+1)U(k+r)$
$w(x) = \frac{d^r u(x)}{dx^r}$	$W(k) = (k+1)(k+2)...(k+r)U(k+r)$
$w(x) = u(x)v(x)$	$W(k) = \sum_{r=0}^{k} U(r)V(k-r)$
$w(x) = \frac{du(x)}{dx}\frac{dv(x)}{dx}$	$W(k) = \sum_{r=0}^{k}(r+1)(k-r+1)U(r+1)V(k-r+1)$
$w(x) = u(x)\frac{dv(x)}{dx}$	$W(k) = \sum_{r=0}^{k}(k-r+1)U(r)V(k-r+1)$
$w(x) = u(x)\frac{d\,v(x)}{dx}\frac{dz(x)}{dx}$	$W(k) = \sum_{r=0}^{k}\sum_{t=0}^{k-r}(t+1)(k-r-t+1) \times U(r)V(t+1)Z(k-r-t+1)$

$$f(z^*) \cong \sum_{i=0}^{N} F(i)(z^* - z^*_0)^i, \tag{29}$$

Eq. (29) implies that $\sum_{i=N+1}^{\infty} F(i)(z^* - z^*_0)^i$ is negligibly small, where N is series size. The fundamental mathematical operations performed by DTM are listed in Table **1**. For brevity we have only documented the DTM procedure for **Case 2** here, as a guide to researchers interested in learning this approach. **Case 1** is considerably simpler than Case 2 in that only a *single differential equation* (7) under boundary conditions (8) requires solution, and therefore details for Case 1 are omitted. Taking the differential transform of Eqs. (18-20), we obtain:

$$(k+1)\rho^*(k+1) = -E_{sl}\sum_{l=0}^{k}(k-l+1)E^*(l)\rho^*(k-l+1) - \frac{\rho^*(k)}{\mathrm{Re}_E} - E_{sl}E_s\sum_{l=0}^{k}\rho^*(l)\rho^*(k-l), \tag{30}$$

$$(k+1)E^*(k+1) = E_s\rho^*(k), \tag{31}$$

$$(k+1)\phi^*(k+1) = -E^*(k). \tag{32}$$

The transform of the boundary conditions are

$$\begin{aligned} &\rho^*[0] = 1, \\ &E^*[0] = 0, \\ &\phi^*[0] = 1. \end{aligned} \tag{33}$$

Therefore the DTM solutions of **equations (18-20)** i.e. ***Case 2 - EHD ion drag flow***, are:

$$\begin{aligned} \rho^*(z^*) \cong\ & 1 + 1.5z^* - 0.517688z^{*2} + 0.297563z^{*3} - 0.095961z^{*4} + 0.0132474z^{*5} \\ & + 0.000654025z^{*6} + 0.000382938z^{*7} - 0.00058118z^{*8} + 0.000137088z^{*9} \\ & + 0.000031461z^{*10} - 0.0000234089z^{*11} + 3.09702\times10^{-6}z^{*12} + 1.53068\times10^{-6}z^{*13} \\ & - 8.28148\times10^{-7}z^{*14} + 1.38651\times10^{-7}z^{*15} + 3.38783\times10^{-8}z^{*16} - 2.86723\times10^{-8}z^{*17} \\ & + 8.22247\times10^{-9}z^{*18} - 2.51079\times10^{-10}z^{*19} - 8.40387\times10^{-10}z^{*20}, \end{aligned} \tag{34}$$

$$\begin{aligned} E^*(z^*) \cong\ & 1 - 2.07075z^* + 1.78538z^{*2} - 0.767688z^{*3} + 0.132474z^{*4} + 0.0078483z^{*5} \\ & + 0.00536113z^{*6} - 0.00929889z^{*7} - 0.0024759z^{*8} + 0.000629219z^{*9} \\ & - 0.000514997z^{*10} - 0.0000743286z^{*11} + 0.0000397976z^{*12} - 0.0000231881z^{*13} \\ & + 4.15954\times10^{-6}z^{*14} + 1.08411\times10^{-6}z^{*15} - 9.74858\times10^{-7}z^{*16} + 2.96009\times10^{-7}z^{*17} \\ & - 9.54101\times10^{-9}z^{*18} - 3.36155\times10^{-8}z^{*19} + 1.66672\times10^{-8}z^{*20}, \end{aligned} \tag{35}$$

$$\begin{aligned} \phi^*(z^*) \cong\ & 1 - 2.07075z^* + 1.78538z^{*2} - 0.767688z^{*3} + 0.132474z^{*4} + 0.0078483z^{*5} \\ & + 0.00536113z^{*6} - 0.00929889z^{*7} - 0.0024759z^{*8} + 0.000629219z^{*9} \\ & - 0.000514997z^{*10} - 0.0000743286z^{*11} + 0.0000397976z^{*12} - 0.0000231881z^{*13} \\ & + 4.15954\times10^{-6}z^{*14} + 1.08411\times10^{-6}z^{*15} - 9.74858\times10^{-7}z^{*16} + 2.96009\times10^{-7}z^{*17} \\ & - 9.54101\times10^{-9}z^{*18} - 3.36155\times10^{-8}z^{*19} + 1.66672\times10^{-8}z^{*20}, \end{aligned} \tag{36}$$

The equations (34-36) have sufficient accuracy, but these series diverge around infinity. As such without using Padé approximants, the analytical solution obtained by DTM, cannot satisfy infinity boundary conditions. It is therefore essential to combine the series solution obtained by DTM with Padé approximants to provide an effective tool to handle boundary value problems on infinite domains.

4. PADÉ APPROXIMANTS

Some techniques exist to increase the convergence of a given series. Among them, the so-called Padé technique is widely applied. Suppose that a function $f(z^*)$ is represented by a power series $\sum_{i=0}^{\infty} c_i z^{*i}$, so that:

$$f(z^*) = \sum_{i=0}^{\infty} c_i z^{*i}. \tag{37}$$

This expansion is the fundamental starting point of any analysis using Padé approximants. The notation c_i, $i = 0, 1, 2, \cdots$ is reserved for the given set of coefficients and $f(z^*)$ is the associated function. $[L, M]$ Padé approximant is a rational fraction given by:

$$\frac{a_0 + a_1 z^* + \cdots + a_L z^{*L}}{b_0 + b_1 z^* + \cdots + b_M z^{*M}}, \tag{38}$$

which has a *Maclaurin expansion* which agrees with (37) as far as possible. Notice that in (38) there are $L+1$ numerator coefficients and $M+1$ denominator coefficients. As a result, there are $L+1$ independent numerator coefficients and *M* independent denominator coefficients, making $L+M+1$ unknown coefficients in all. This number suggests that normally $[L, M]$ ought to fit the power series (37) through the orders $1, z^*, z^{*2}, \cdots, z^{*L+M}$. In the notation of formal power series:

$$\sum_{i=0}^{\infty} c_i z^{*i} = \frac{a_0 + a_1 z^* + \cdots + a_L z^{*L}}{b_0 + b_1 z^* + \cdots + b_M z^{*M}} + O\left(z^{*L+M+1}\right), \tag{39}$$

Baker and Graves-Morris show [45] have identified that:

$$\begin{aligned} &\left(b_0 + b_1 z^* + \cdots + b_M z^{*M}\right)(c_0 + c_1 z^* + \cdots) = \\ &a_0 + a_1 z^* + \cdots + a_L z^{*L} + Oz^*\left(\eta^{L+M+1}\right) \end{aligned} \tag{40}$$

Equating the coefficients of $\eta^{L+1}, \eta^{L+2}, \cdots, \eta^{L+M}$

$$\begin{aligned} &b_M c_{L-M+1} + b_{M-1}c_{L-M+2} + \cdots + b_0 c_{L+1} = 0, \\ &b_M c_{L-M+2} + b_{M-1}c_{L-M+3} + \cdots + b_0 c_{L+2} = 0, \\ &\vdots \\ &b_M c_L + b_{M-1}c_{L+1} + \cdots + b_0 c_{L+M} = 0, \end{aligned} \tag{41}$$

If $i \prec 0$, we define $c_i = 0$ for consistency. Since $b_0 = 1$, Eq. (41) becomes a set of M *linear* equations for the M unknown denominator coefficients:

$$\begin{pmatrix} c_{L-M+1} & c_{L-M+2} & c_{L-M+3} & \cdots & c_L \\ c_{L-M+2} & c_{L-M+3} & c_{L-M+4} & \cdots & c_{L+1} \\ c_{L-M+3} & c_{L-M+4} & c_{L-M+5} & \cdots & c_{L+2} \\ \vdots & \vdots & \vdots & \vdots & \\ c_L & c_{L+1} & c_{L+2} & \cdots & c_{L+M-1} \end{pmatrix} \begin{pmatrix} b_M \\ b_{M-1} \\ b_{M-2} \\ \vdots \\ b_1 \end{pmatrix} = - \begin{pmatrix} c_{L+1} \\ c_{L+2} \\ c_{L+3} \\ \vdots \\ c_{L+M} \end{pmatrix}, \quad (42)$$

From these equations, *b* values may be found. The numerator coefficients, $a_0, a_1, \cdots, a_L$, follow immediately from (40) by equating the coefficients of $1, z^*, z^{*2}, \cdots, z^{*L+M}$:

$$\begin{aligned} a_0 &= c_0, \\ a_1 &= c_1 + b_1 c_0, \\ a_2 &= c_2 + b_1 c_1 + b_2 c_0, \\ &\vdots \\ a_L &= c_L + \sum_{i=1}^{\min\{L,M\}} b_i c_{L-i}. \end{aligned} \quad (43)$$

Thus (42) and (43) normally determine the Padé numerator and denominator and are called the *Padé equations*. The $[L, M]$ Padé approximant is constructed which agrees with $\sum_{i=0}^{\infty} c_i z^{*i}$, through order z^{*L+M}. The order of Padé approximants $[L, M]$, [6, 6] has sufficient accuracy; on the other hand, if the order of the Padé approximation increases, the accuracy of the solution increases. Further extensive details of Padé approximants are provided in Baker and Graves-Morris [45], Baker [46], Rashidi [47] and Bég [48]. In light of the above details, the [6, 6] Padé approximants for **Case 2** i.e. eqns. (34) and (35), and the [5, 5] Padé approximants of (36) are as follows:

$$\begin{aligned} \rho^*(z^*)_{[6,6]} = (&1 + 2.22184z^* + 0.910821z^{*2} + 0.538894z^{*3} + 0.103521z^{*4} \\ &+ 0.027358z^{*5} + 0.00179448z^{*6} + 0.000367531z^{*7} \\ &- 0.00009861z^{*8} - 0.000071155z^{*9} + 0.0000164646z^{*10}) / (1 \\ &+ 0.721841z^* + 0.345747z^{*2} + 0.0963992z^{*3} + 0.0190791z^{*4} \\ &+ 0.00178378z^{*5} - 0.000316272z^{*6} - 0.0000965818z^{*7} \\ &- 0.0000158136z^{*8} + 2.08519\times10^{-6} z^{*9} + 1.04034\times10^{-6} z^{*10}), \end{aligned} \quad (44)$$

$$\begin{aligned} E^*(z^*)_{[6,6]} = (&1 - 0.97484z^* + 0.314109z^{*2} - 0.0641004z^{*3} + 0.0501699z^{*4} \\ &- 0.0285218z^{*5} + 0.00705916z^{*6} - 0.000778593z^{*7} \\ &+ 0.000102791z^{*8} - 0.0000347496z^{*9} + 4.52094\times10^{-6} z^{*10}) / (1 \\ &+ 1.09607z^* + 0.798418z^{*2} + 0.400019z^{*3} + 0.161998z^{*4} \\ &+ 0.0526388z^{*5} + 0.0141896z^{*6} + 0.00315306z^{*7} \\ &+ 0.00055245z^{*8} + 0.0000743182z^{*9} + 6.16186\times10^{-6} z^{*10}). \end{aligned} \quad (45)$$

$$\begin{aligned} \phi^*(z^*)_{[5,5]} = (&1 - 0.97484z^* + 0.314109z^{*2} - 0.0641004z^{*3} + 0.0501699z^{*4} \\ &- 0.0285218z^{*5} + 0.00705916z^{*6} - 0.000778593z^{*7} \\ &+ 0.000102791z^{*8} - 0.0000347496z^{*9} + 4.52094\times10^{-6} z^{*10}) / (1 \\ &+ 1.09607z^* + 0.798418z^{*2} + 0.400019z^{*3} + 0.161998z^{*4} \\ &+ 0.0526388z^{*5} + 0.0141896z^{*6} + 0.00315306z^{*7} \\ &+ 0.00055245z^{*8} + 0.0000743182z^{*9} + 6.16186\times10^{-6} z^{*10}). \end{aligned} \quad (46)$$

For both Cases 1 and 2, numerical shooting quadrature solutions have also been obtained to further validate the DTM-Padé solutions. These employ 4th order Runge-Kutta integration schemes and further details are given in Rashidi [47] and Bég [48].

5. COMPUTATIONS AND DISCUSSION

Detailed solutions generated by the **DTM-Padé** simulation are presented. We consider Case 1 first and then discuss solutions obtained for Case 2.

Case 1: Electrohydrodynamic Ion Drag Flow in a Circular Cylindrical Conduit

The influence of electrical Hartmann number (Ha_e^2) and non-linearity parameter (α) on the axial velocity (W^*) evolution with radial coordinate (r^*) are depicted in Figures **3** to **14**. In these plots the **DTM-Padé** solutions correspond to solid lines and we have compared our computations with numerical shooting quadrature method. In all cases the correlation is excellent. It is apparent from Figures **3** to **8** that as α is increased, there is a strong decrease in axial velocity at the inlet ($r^* = 0$). As square of electrical Hartmann number increases from Figure **3** ($Ha^2_e = 0.5$), through Figure **4** ($Ha^2_e = 2$), Figure **5** ($Ha^2_e = 4$), Figure **6** ($Ha^2_e = 6$), Figure **7** ($Ha^2_e = 8$) and Figure **8** ($Ha^2_e = 10$), magnitudes of the axial velocity are markedly *elevated*. With higher Ha^2_e values, velocity profiles are also progressively flattened towards the start of of the conduit i.e. $r^* = 0$. $Ha_e = \sqrt{\frac{j_0 a^2}{\mu K^2 E_0}}$ and embodies the relative effect of the in the *electrical Coulomb force* and the *viscous* force in the regime. Greater electrical Hartmann number will induce a decrease in viscous force and an elevation in electrical force. Ha_e is also directly proportional to current density (uniform over the cross-section at the pump conduit inlet). *Greater* acceleration of the flow is caused with higher electrical Coulomb force. In all cases the fluid velocity vanishes at the end (exit point) of the conduit, in accordance with the boundary condition specified there ($W^* \rightarrow 0$ *as* $r^* \rightarrow 1$). 9 to 14, where a strong escalation in axial velocity accompanies a rise in electrical Hartmann number. An increase in non-linearity parameter (α) is again observed to depress velocities. These trends are further observed in Figures **9** to **14**. Furthermore the

DTM-Padé solutions computed in Figures **3-14** show excellent agreement with the perturbation computations of McKee *et al.* [39] and the homotopy computations of Mastroberardino [15]. Excellent confidence in the present solutions is further demonstrated with the numerical quadrature comparisons in all Figures **3-14**. Confidence in the present computations is therefore high.

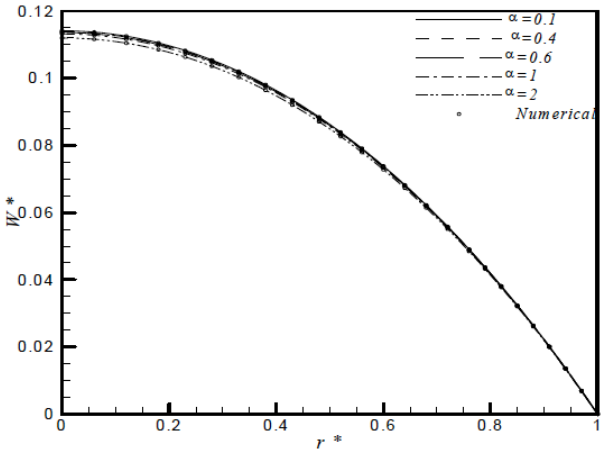

Figure 3: Axial flow velocity variation with various α for $Ha_e^2 = 0.5$.

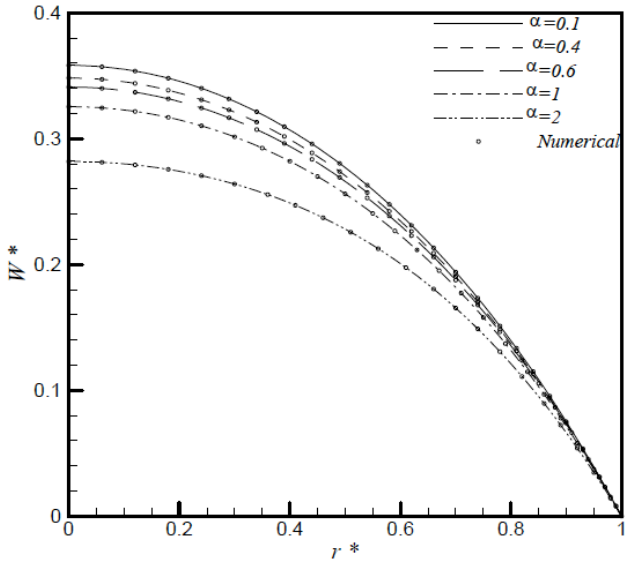

Figure 4: Axial flow velocity variation with various α for $Ha_e^2 = 2$.

Case 2: Unipolar DC EHD Pump Flow

In this second test problem, for which details of the **DTM-Padé** procedure were given, we examine the effects of three electrohydrodynamic control parameters: electrical slip number (E_s), electrical source number (E_s) and electrical Reynolds number

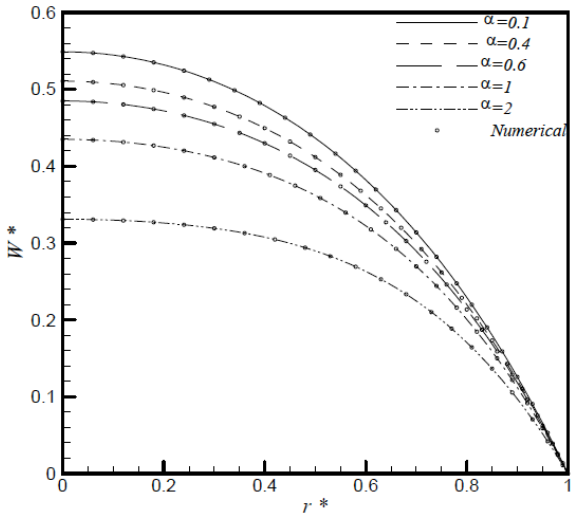

Figure 5: Axial flow velocity variation with various α for $Ha_e^2 = 4$.

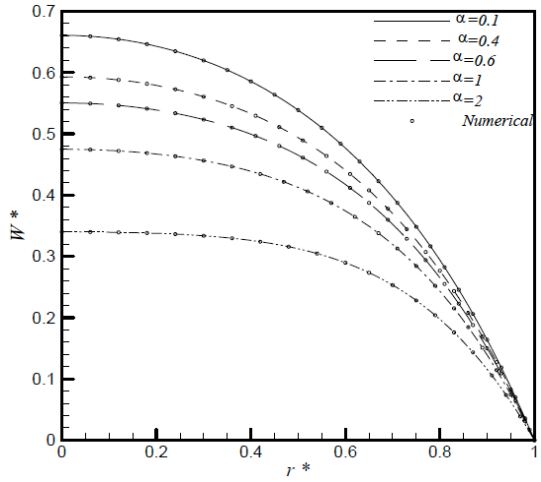

Figure 6: Axial flow velocity variation with various α for $Ha_e^2 = 6$.

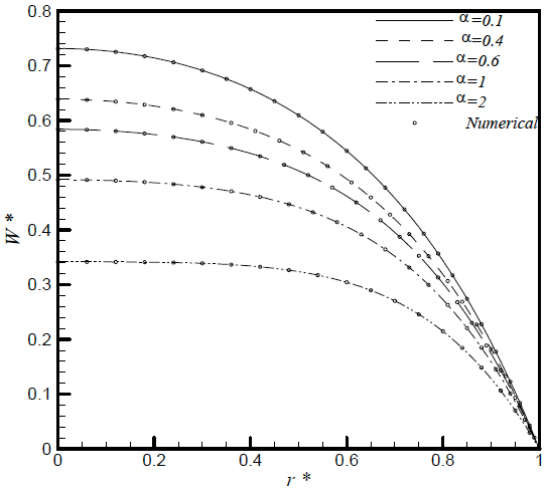

Figure 7: Axial flow velocity variation with various α for $Ha_e^2 = 8$.

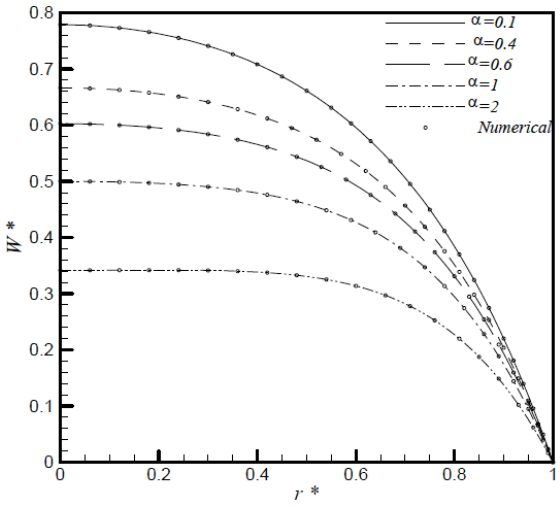

Figure 8: Axial flow velocity variation with various α for $Ha_e^2 = 10$.

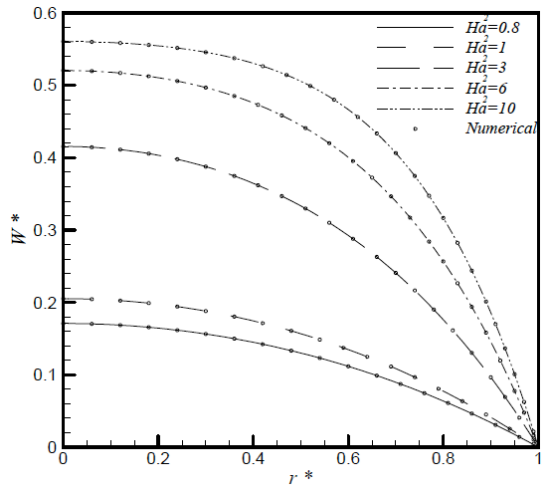

Figure 11: Axial flow velocity variation with various Ha_e^2 for $\alpha = 0.75$.

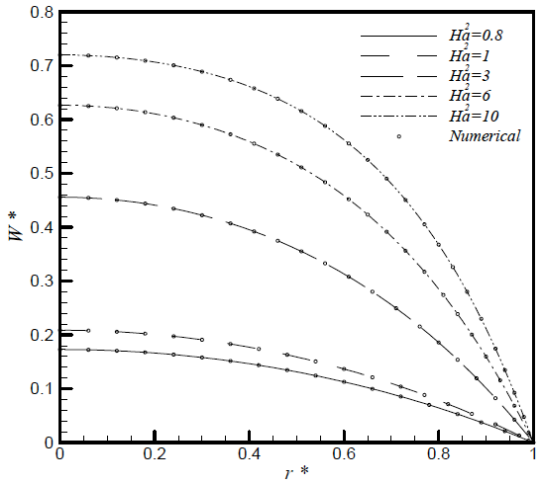

Figure 9: Axial flow velocity variation with various Ha_e^2 for $\alpha = 0.25$.

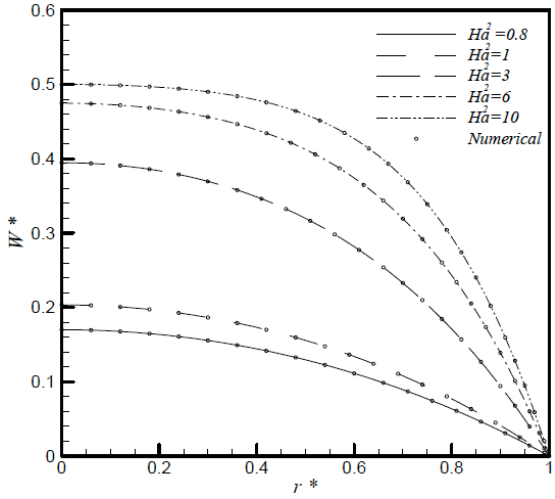

Figure 12: Axial flow velocity variation with various Ha_e^2 for $\alpha = 1$.

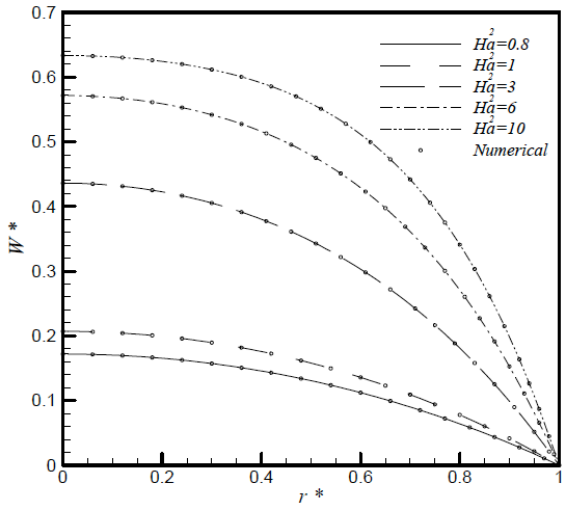

Figure 10: Axial flow velocity variation with various Ha_e^2 for $\alpha = 0.5$.

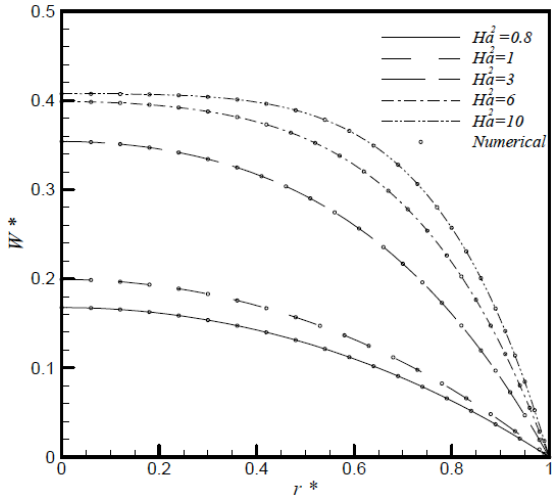

Figure 13: Axial flow velocity variation with various Ha_e^2 for $\alpha = 1.5$.

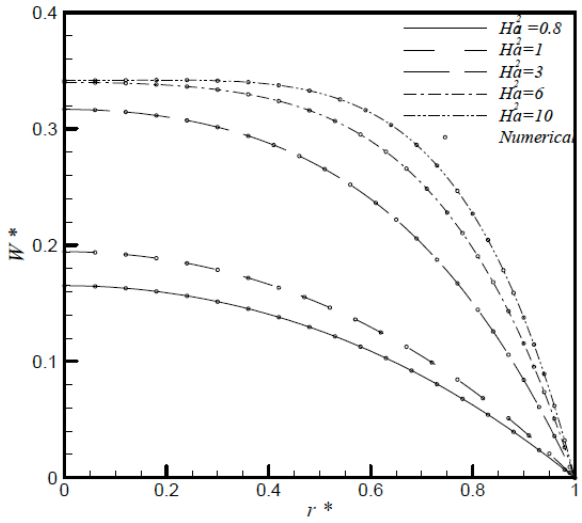

Figure 14: Axial flow velocity variation with various Ha_e^2 for $\alpha = 2$.

(Re_e) on the electrical field (E^*), potential (ϕ^*), and charge density (ρ^*) distributions. To validate the present **DTM-Padé** solutions, we have compared our computations with several numerical solutions obtained with the 4th order shooting quadrature method. Additionally we have shown DTM computations in the absence of Padé approximants. Inspection of Figures **15** to **18** and Table **2** to **4** shows that generally excellent correlation is achieved between DTM-Padé and numerical quadrature. However the *deviation* of solutions corresponding to the classical DTM approach is clearly evident. The necessity for incorporating Padé approximants is therefore clearly demonstrated. The DTM solutions for dimensionless charge density (Figure **15**) diverge from the correct numerical solution at an intermediate distance along the conduit length, *z* ~ 0.44*. The DTM-Padé solutions exactly replicate the numerical quadrature solution throughout the conduit length i.e. there is never any deviation in solutions when Padé approximants are utilized. Divergence in DTM solutions for electrical field (Figure **16**) and dimensionless potential (Figure **17**) also arise in the intermediate region of the conduit length but progressively further along. Figure **18** demonstrates that the relative error between the DTM-Padé and numerical shooting solutions is almost indistinguishable. Further we note that the [*L, M*] Padé approximants in Tables **2-4** and Figures **15-18**, were selected as [3, 3], [4, 4] and [5, 5], [6, 6] for the flow variables, as expressed in eqns. (44) to (46).

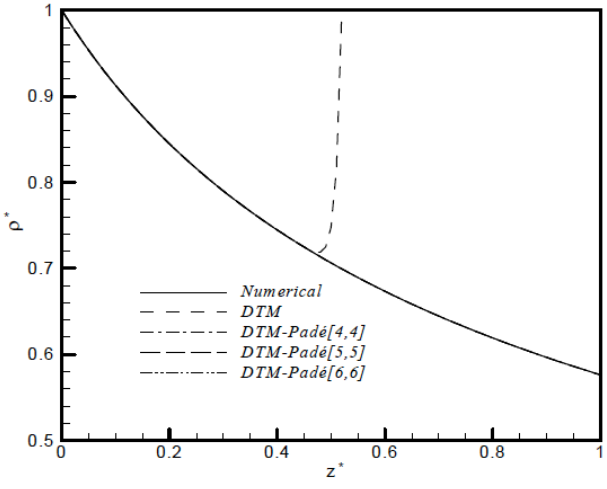

Figure 15: Dimensionless charge density (ρ^*) obtained by DTM, DTM–Padé and numerical shooting quadrature with $E_s = 1, E_{sl} = 1, Re_e = 350$.

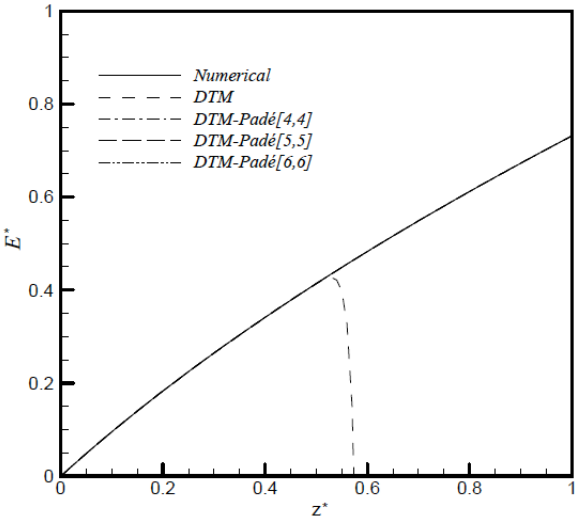

Figure 16: Dimensionless electrical field (E^*) obtained by DTM, DTM–Padé and numerical shooting quadrature with $E_s = 1, E_{sl} = 1, Re_e = 350$.

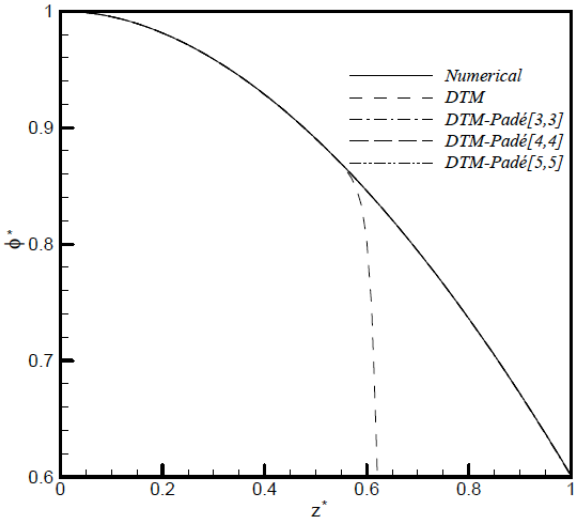

Figure 17: Dimensionless potential (ϕ^*) obtained by DTM, DTM–Padé and numerical shooting quadrature with $E_s = 1, E_{sl} = 1, Re_e = 350$.

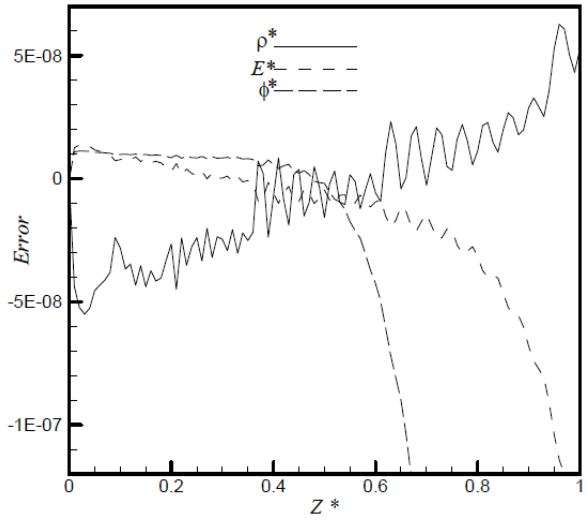

Figure 18: The error between DTM–Padé and numerical shooting quadrature for electrical field (E^*), potential (ϕ^*), and charge density (ρ^*) with $E_s = 1, E_{sl} = 1, Re_e = 350$.

Figures **19** to **21** show that the charge density ρ^* and potential ϕ^* are strongly decreased whereas electrical field E^* is increased with an increase in the values of E_s. Charge density profiles (Figure **19**) are seen to be maximized at the conduit inlet and minimized at the outlet. The opposite is observed for the electrical field in Figure **20**. Figure **21** further reveals that electrical potential vanishes at the conduit outlet for E_S values of 0.5, 1 and 3; however with higher E_S values, the electrical potential is found to vanish systematically closer to the inlet. For example, for E_S = 10, $\phi^* \rightarrow 0$ *at* Z^* ~ 0.85, for E_S= 25 at Z^* ~ 0.625 and for E_S = 50 at Z^* ~ 0.5. This has not been observed in previous studies e.g. Bég *et al.* [14] and Seyed-Yagoobi *et al.* [40], since these other numerical investigations did not consider sufficiently high values of the electrical source number. E_S is based on the analogy between *thermal conduction* (Fourier's equation) and *electrostatics* (Poisson's equation). The *ratio of heat source (W/m^3) to thermal conductivity*

Table 2: (ρ^*) **Obtained by DTM–Padé and Numerical Quadrature for** $E_s = 1, E_{sl} = 1, Re_e = 350$

Numerical	DTM–Padé [6,6]	DTM–Padé [5,5]	DTM–Padé [4,4]	DTM–Padé	Z^*
1.	1.	1.	1.	1.	0.
0.912633	0.912633	0.912633	0.912633	0.912633	0.1
0.844744	0.844744	0.844744	0.844744	0.844744	0.2
0.79003	0.790029	0.790029	0.790029	0.790031	0.3
0.744713	0.744713	0.744713	0.744713	0.745361	0.4
0.706381	0.706381	0.706381	0.706381	0.769633	0.5
0.673405	0.673405	0.673405	0.673405	3.32158	0.6
0.644643	0.644643	0.644643	0.644644	62.5066	0.7
0.619269	0.619269	0.619269	0.619272	944.284	0.8
0.596665	0.596665	0.596666	0.59667	10402.6	0.9
0.576363	0.576363	0.576363	0.576371	88778.3	1

Table 3: (E^*) **Obtained by DTM–Padé and Numerical Quadrature for** $E_s = 1, E_{sl} = 1, Re_e = 350$

Numerical	DTM–Padé [6,6]	DTM–Padé [5,5]	DTM–Padé [4,4]	DTM–Padé	Z^*
0	0.	0.	0.	0.	0.
0.0954325	0.0954325	0.0954325	0.0954325	0.0954325	0.1
0.18317	0.18317	0.18317	0.18317	0.18317	0.2
0.264818	0.264818	0.264818	0.264818	0.264818	0.3
0.341488	0.341488	0.341488	0.341488	0.341472	0.4
0.413992	0.413992	0.413992	0.413992	0.412414	0.5
0.482942	0.482942	0.482942	0.482941	0.416711	0.6
0.548814	0.548814	0.548813	0.54881	-1.00133	0.7
0.611984	0.611984	0.611983	0.611977	-23.073	0.8
0.67276	0.672759	0.672759	0.672746	-260.773	0.9
0.731393	0.731393	0.731392	0.731369	-2233.35	1

Table 4: (ϕ^*) **Obtained by DTM–Padé and Numerical Quadrature for** $E_s = 1, E_{sl} = 1, Re_e = 350$

Numerical	DTM–Padé [5,5]	DTM–Padé [4,4]	DTM–Padé [3,3]	DTM–Padé	Z^*
{1.}	1.	1.	1.	1.	0.
{0.995156}	0.995156	0.995156	0.995156	0.995156	0.1
{0.981169}	0.981169	0.981169	0.981169	0.981169	0.2
{0.958724}	0.958724	0.958724	0.958723	0.958724	0.3
{0.928371}	0.928371	0.928371	0.928366	0.928371	0.4
{0.890565}	0.890565	0.890565	0.890548	0.890524	0.5
{0.845691}	0.845691	0.845689	0.845641	0.843948	0.6
{0.794079}	0.794079	0.794075	0.793962	0.753212	0.7
{0.736018}	0.736018	0.736007	0.735774	0.110524	0.8
{0.671762}	0.671761	0.671739	0.671304	-6.24303	0.9
{0.601538}	0.601535	0.601492	0.600739	-58.5633	1

(W/mK) i.e. q'/k in Fourier's law is analogous to the *ratio of space charge density to electrical permittivity (ρ/ε)* in Poisson's equation. The electrical source parameter therefore exerts a significant effect on all variables in EHD ion drag flow. The numerical quadrature solutions again show excellent correlation with the DTM-Padé computations in Figures **19** to **21**.

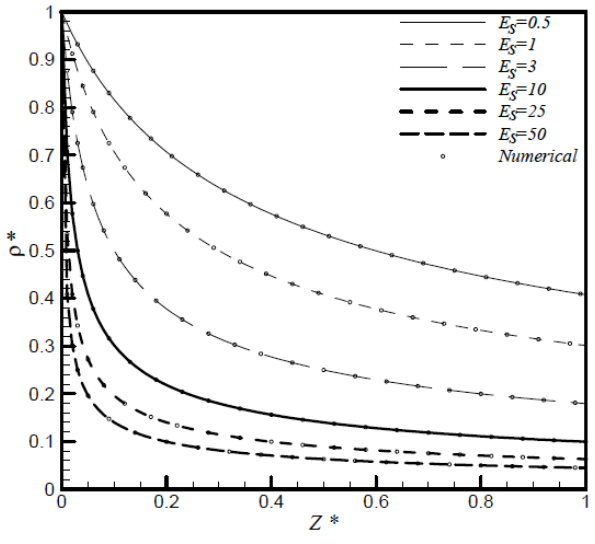

Figure 19: Charge density (ρ^*) versus axial coordinate (Z^*) for various E_s with $Re_e = 350, E_{sl} = 5$.

Figures **22** to **24** illustrate the influence of the electrical Reynolds number, *Re*, on charge density ρ^*, electrical field E^* and potential ϕ^*. *Re* symbolizes the relative influence of charge convection effect and is the ratio of the timescales of charge convection by flow to that for charge relaxation by ohmic conduction. Evidently, increasing electrical Reynolds number from 1 to 30 results in a major escalation in *charge density*. However for subsequent enhancement in electrical Reynolds number, there is no tangible change in charge density (Figure **22**). This implies that there is a critical limit to the charge density which can be generated in ion drag flow in the system, and a finite limit to the influence of the charge convection effect as simulated in electrical Reynolds number. Figure **23** indicates that an increase in electrical Reynolds number also enhances the electrical field in the conduit. For *Re* = 1 the profile is a monotonic growth; however for Re values greater than 30 and up to 600), the profile evolves into a linear growth. There is no noticeable variation in electrical field between *Re* = 30 and *Re* = 600, again indicating that the charge convection effect has a limit and cannot generate

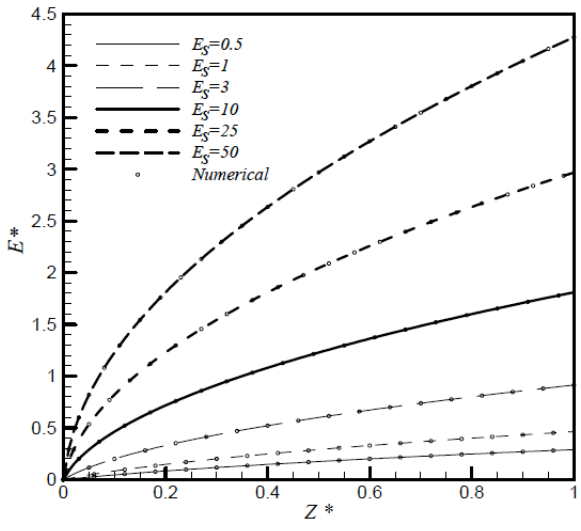

Figure 20: Electrical field (E^*) versus axial coordinate (Z^*) for various E_s with $Re_e = 350, E_{sl} = 5$.

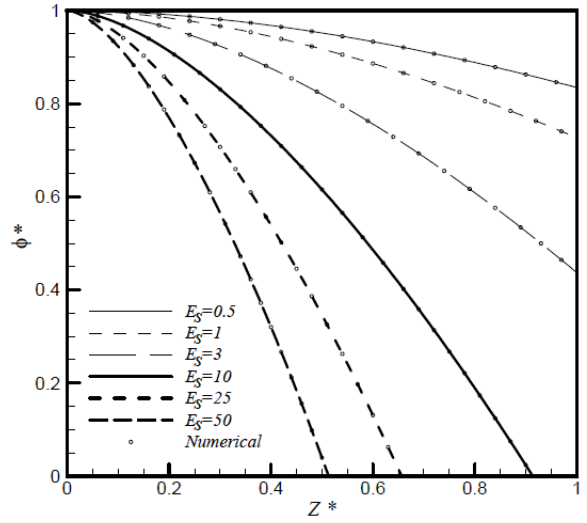

Figure 21: Potential (ϕ^*) versus axial coordinate (Z^*) for various E_s with $Re_e = 350, E_{sl} = 5$.

electrical field increase beyond a critical point. Electrical potential is found to conversely decrease with increasing electrical Reynolds number, as seen in Figure **24**. As indicated earlier, however there is no significant further decrease beyond electrical Reynolds number of 30. For all cases in Figure **24**, the profiles exhibit a monotonic decay. Even at very high electrical Reynolds numbers, the charge density is found to vanish at the end of the conduit, as is apparent at the lowest electrical Reynolds number.

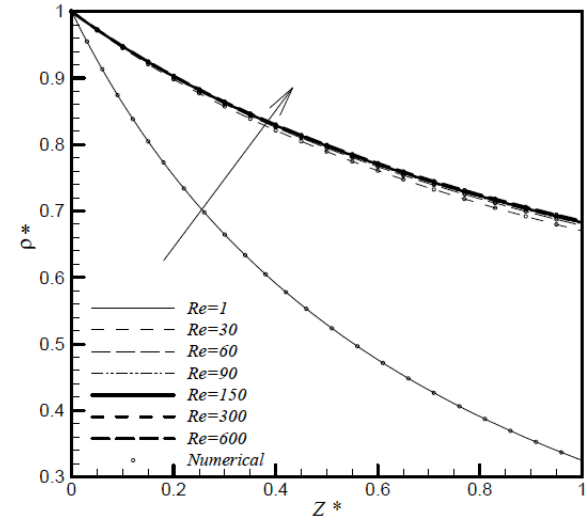

Figure 22: Charge density (ρ^*) versus axial coordinate (Z^*) for various Re with $E_s = E_{sl} = 0.75$.

Figures **25** to **27** illustrate the influence of the electrical slip number, E_{sl} on charge density ρ^*, electrical field E^* and potential ϕ^*. The *electrical slip number* quantifies the relative motion of the injected

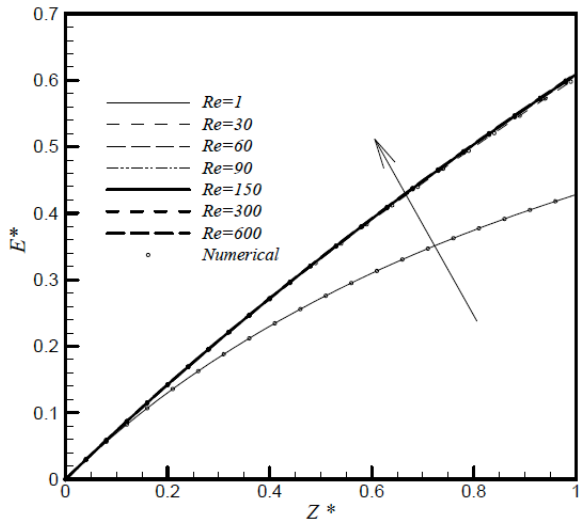

Figure 23: Electrical field (E^*) versus axial coordinate (Z^*) for various Re with $E_s = E_{sl} = 0.75$.

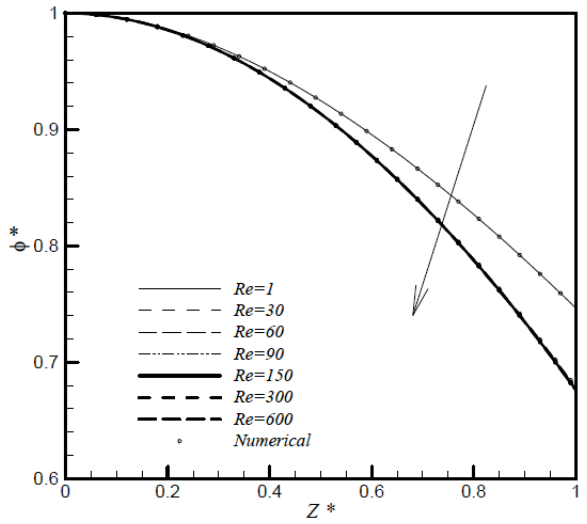

Figure 24: Electrical potential (ϕ^*) versus axial coordinate (Z^*) for various Re with $E_s = E_{sl} = 0.75$.

charges with regard to the bulk fluid velocity (*u*). $E_{sl} = 0$ relates to the scenario wherein there is no *zero contribution of the mobility component to the current density,* as indicated earlier by Bég *et al.* [14]. A distinct decrease in charge density is induced with an increase in electrical slip number, as seen in Figure **25**. Profiles also increasingly evolve from approximately linear decay for $E_{sl} = 0.7$ to a very strong monotonic decay for $E_{sl} = 20$. Similar trends were observed by Seyed-Yagoobi *et al.* [40] although they did not consider electrical slip number values beyond 5. In Figure **26**, electrical field is also found to be strongly decreased with a rise in electrical slip numbers. The profiles evolve from a strong linear growth for $E_{sl} = 0.7$ to a strong monotonic growth for $E_{sl} = 20$. A very different response to increasing electrical slip number is

observed in Figure **27** where electrical potential is seen to be considerably elevated with an increase in E_{sl} from 0.7 through 1, 2, 10 to 20. Figures **25-27** all correspond to very high electrical Reynolds number (400) and again exhibit excellent correlation between the **DTM-Padé** semi-numerical and the 4th order Runge-Kutta numerical quadrature solutions. Stable, convergent solutions are clearly achieved testifying to the excellent ability and accuracy of the **DTM-Padé** semi-numerical simulation.

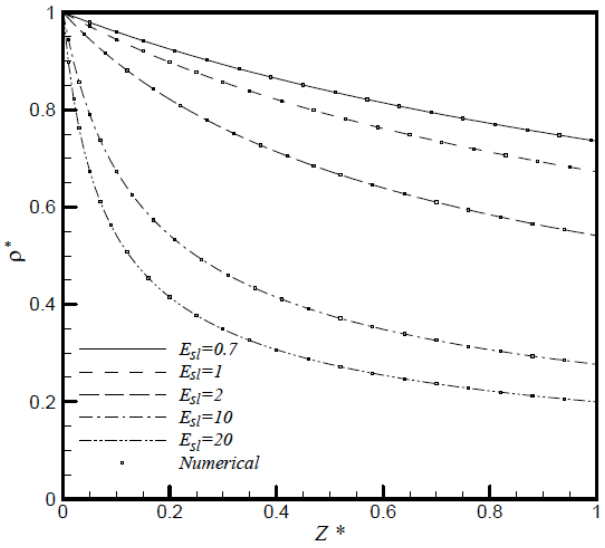

Figure 25: Charge density (ρ^*) versus axial coordinate (Z^*) for various E_{sl} with $Re_e = 400, E_s = 0.6$.

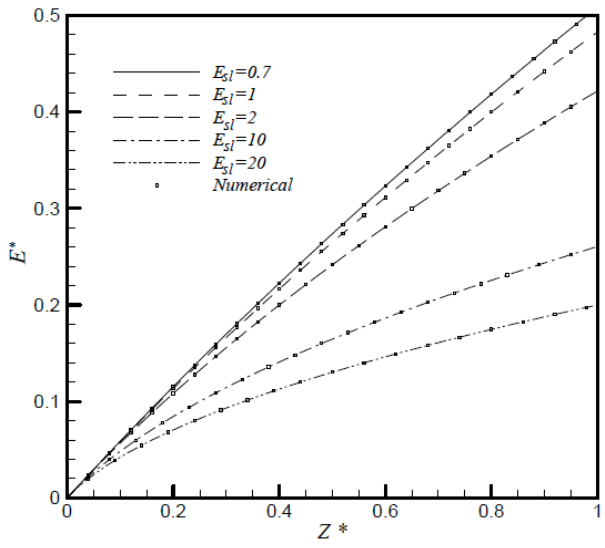

Figure 26: Electrical field (E^*) versus axial coordinate (Z^*) for various E_{sl} with $Re_e = 400, E_s = 0.6$.

Finally Figures **28** to **30** illustrate the evolution of ion drag pump power efficiency, η_{EHD} with variation in

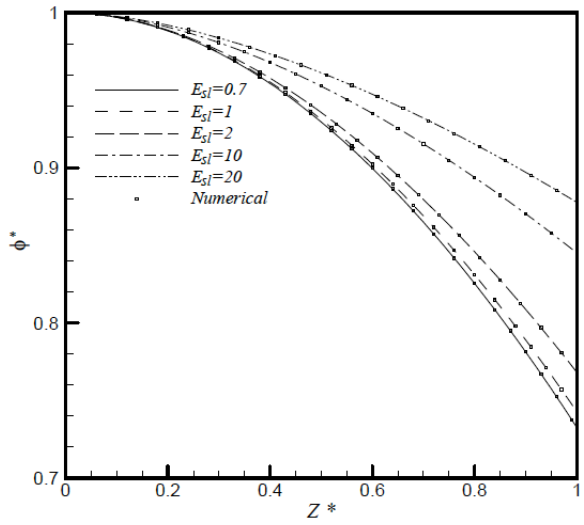

Figure 27: Potential (ϕ^*) versus axial coordinate (Z^*) for various E_{sl} with $Re_e = 400, E_s = 0.6$.

Re_e, E_s and E_{sl}. $\eta = \dfrac{\frac{1}{2}E^{*2}_L}{Es[1-\Phi^*_L]}$ and, as elaborated earlier, this definition for efficiency shows clearly the relationship with electrical field values at the emitter and the collector electrodes. The effect of electrical Reynolds number is found to be small (Figure **28**). Peak efficiency is reached very quickly as electrical Reynolds number increases. There is a much more prominent influence however observed on efficiency by the electrical slip number. For E_{sl} = 100, efficiency peaks at about 13%; however this is hugely boosted with *decreasing* electrical slip numbers and for E_{sl} = 1, the maximum efficiency attained is 33%. Therefore by altering the electrical slip number the ion drag EHD

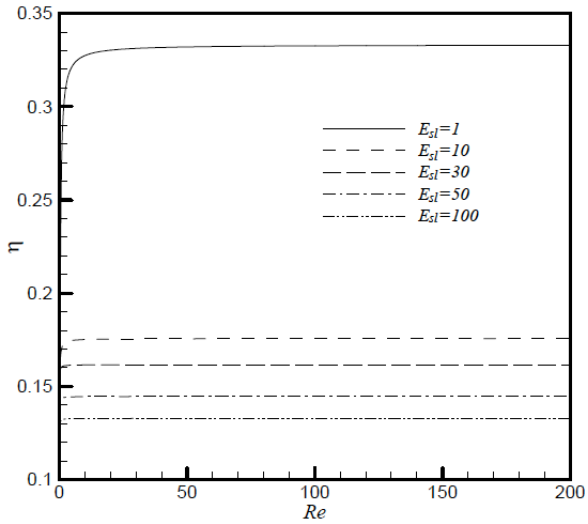

Figure 28: Distribution of η_{ehd} versus Re_e for E_s = 10 and for various E_{sl} values.

pump efficiency can be massively increased. Figure **29** shows that a very slight increase in pump efficiency is caused by an increase in electrical Reynolds numbers from 1 to 600. However a very strong decrease in efficiency is observed with an increase in the electrical slip number, confirming the trends observed in Figure **28**. Figure **30** further shows that increasing electrical Reynolds number induces a minor enhancement in efficiency whereas a significant decrease in efficiency is induced with increasing electrical source numbers. Peak efficiency is therefore computed for both *very low electrical slip* and *electrical source* numbers.

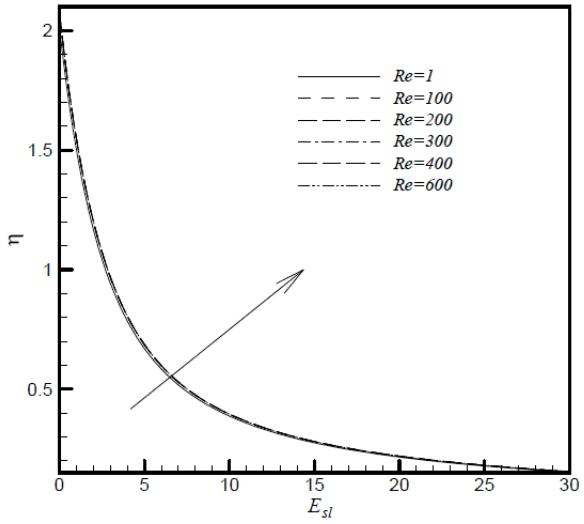

Figure 29: Distribution of η_{ehd} versus E_{sl} for E_s = 10 and for various Re_e values.

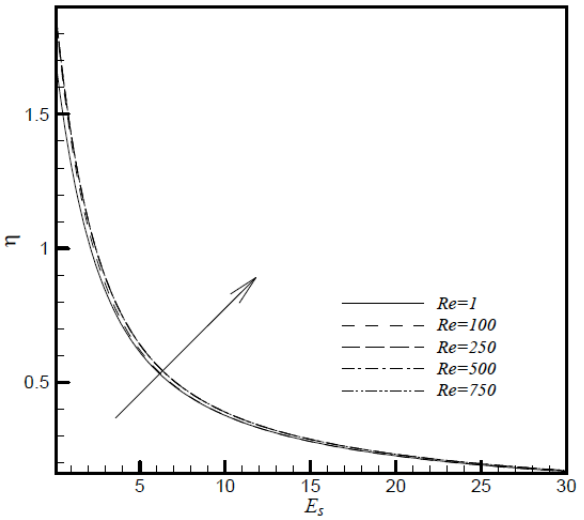

Figure 30: Distribution of η_{ehd} versus E_s for E_{sl} = 3 and for various Re_e values.

6. CONCLUSIONS

A detailed semi-numerical study has been conducted of several electrohydrodynamic flows of relevance to ion drag pump systems using the differential transform method (DTM) and also the combined DTM-Padé simulation. For both test problems examined excellent correlation has been achieved between numerical quadrature solutions (4th order Runge Kutta method) and DTM-Padé solutions. However significant divergence of solutions has been identified with DTM. Extensive details of the selection of Padé approximants necessary for sustaining converged solutions are also documented. An error analysis has also been conducted. The results have generally confirmed, but also extended the range of electrohydrodynamic parameters considered in previous numerical studies. Key parameters influencing the optimization of EHD pump efficiency and also flow acceleration have been identified. The current study shows that DTM-Padé simulation holds excellent promise in simulating nonlinear electrohydrodynamic problems and also provides researchers with an alternative technique with which they can benchmark solutions generated by more conventional numerical methods such as finite element and network simulation methods, and also purely analytical methods such as the homotopy analysis method. Future studies will examine electro-rheological flows and also employ DTM-Padé simulation in thin film electrohydrodynamics [49].

ACKNOWLEDGEMENTS

The authors are grateful to the referee for his comments which have served to improve the article.

REFERENCES

[1] Zamankhan P, Ahmadi G, Fan F-G. Coupling effects of the flow and electric fields in electrostatic precipitators. J Appl Phys 2004; 96: 7002-10. http://dx.doi.org/10.1063/1.1810201

[2] Yeh S-R, Seul M, Shraiman BI. Assembly of ordered colloidal aggregates by electric-field-induced fluid flow. Nature 1997; 386: 57-9. http://dx.doi.org/10.1038/386057a0

[3] Driouich M, Gueraoui K, Sammouda M, Haddad YM, Aberdane I. The effect of electric field on the flow of a compressible ionized fluid in a cylindrical tube. Adv Studies Theor Phys 2012; 6: 687-96.

[4] Green NG, Ramos A, Gonzalez A, Morgan H, Castellanos A. Fluid flow induced by non-uniform AC electric fields in electrolytes on microelectrodes III: Observation of streamlines and numerical simulation. Phys Rev E 2002; 66: 026305. http://dx.doi.org/10.1103/PhysRevE.66.026305

[5] Hou M, Chen W, Zhang T, Lu K. Electric field controlled dilute–dense flow transition in granular flow through a vertical pipe. Powder Technol 2003; 43: 135-6.

[6] Chankin AV, Coster DP, Asakura N, *et al*. A possible role of radial electric field in driving parallel ion flow in scrape-off layer of divertor tokamaks. Nucl Fusion 2007; 47: 762. http://dx.doi.org/10.1088/0029-5515/47/8/006

[7] Zake M, Purmals M, Lubane M. Enhanced electric field effect on a flame. J Enhanced Heat Transfer 1998; 5: 139-63.

[8] Cao JG, Huang JP, Zhou LW. Structure of electrorheological fluids under an electric field and a shear flow: experiment and computer simulation. J Phys Chem B 2006; 110: 11635-9. http://dx.doi.org/10.1021/jp0611774

[9] Naqwi AA, Hartman RPA, Marijnissen JCM. Basic studies of electrohydrodynamic atomization process using phase Doppler measurement technique. Part Part Syst Char 1996; 13: 143-9l.

[10] Lao AIK, Trau D, Hsing I-M. Miniaturized flow fractionation device assisted by a pulsed electric field for nanoparticle separation. Anal Chem 2002; 74: 5364-9. http://dx.doi.org/10.1021/ac0257647

[11] Choi HK, Park J-U, Park OO, Ferreira PM, Georgiadis JG, Rogers JA. Scaling laws for jet pulsations associated with high resolution electrohydrodynamic printing. Appl Phys Lett 2008; 92: 123109. http://dx.doi.org/10.1063/1.2903700

[12] Lenguito G, de la Mora F, Gomez A. Multiplexed electrospray for space propulsion applications, 46th AIAA Joint Propulsion Conference, AIAA-2010-6521, Caltech, Pasadena 2010.

[13] Roth JR, Sin H, Madhan R, Wilkinson S. Flow re-attachment and acceleration by paraelectric and peristaltic electrohydrodynamic effects. 41st Aerospace Sciences Meeting and Exhibit, Reno, Nevada, AIAA Paper 2003-531, 2003.

[14] Bég OA, Zueco J, Bég TA, Bhargava R. Network simulation of the electrohydrodynamic ion drag energy pump with electrical Reynolds number, slip and source effects. Int J Appl Math Mech 2010; 6: 78-95.

[15] Mastroberardino A. Homotopy analysis method applied to electrohydrodynamic flow. Commun Nonlinear Sci Numer Sim 2011; 16: 2730-6. http://dx.doi.org/10.1016/j.cnsns.2010.10.004

[16] Chen X, Cheng J, Yin X. Numerical analysis of electrohydrodynamics in a round pipe. IEEE T Dielect El In 2003; 10: 278-84. http://dx.doi.org/10.1109/TDEI.2003.1194111

[17] Fengt JQ, Scott TC. A computational analysis of electrohydrodynamics of a leaky dielectric drop, in an electric field. J Fluid Mech 1996; 311: 289-326. http://dx.doi.org/10.1017/S0022112096002601

[18] Vázquez PA, Georghiou GE, Castellanos A. Characterization of injection instabilities in electrohydrodynamics by numerical modelling: comparison of particle in cell and flux corrected transport methods for electroconvection between two plates. J Phys D Appl Phys 2006; 39: 2754. http://dx.doi.org/10.1088/0022-3727/39/13/019

[19] Xuan ZC, Zhang XK. Simulation of Stokes flow over microelectrodes with least squares meshfree method. Simul Model Pract Th 2008; 16: 294-314. http://dx.doi.org/10.1016/j.simpat.2007.11.012

[20] Verplaetsen F, Berghmans JA. Study of the influence of an electric field on the liquid-vapor interface during film boiling of stagnant fluids. IEEE T Ind Appl 1997; 33: 1512-8. http://dx.doi.org/10.1109/28.649963

[21] Lean M, Domoto G. Electrohydrodynamics of charge transport in Stoke's flow. IEEE T Magn 1987; 23: 2656-9. http://dx.doi.org/10.1109/TMAG.1987.1065696

[22] Kupershtokh AL, Medvedev DA. Lattice Boltzmann equation method in electrohydrodynamic problems. J Electrostat 2006; 64: 581-5. http://dx.doi.org/10.1016/j.elstat.2005.10.012

[23] Van Poppel BP. Numerical methods for simulating multiphase electrohydrodynamic flows with application to liquid fuel injection. PhD Thesis, University of Colorado at Boulder, USA 2010; p. 144.

[24] Grandison S, Vanden-Broeck J-M, Papageorgiou DT, Miloh T, Spivak B. Ax symmetric waves in electrohydrodynamic flows. J Eng Math 2007; 62: 133-48. http://dx.doi.org/10.1007/s10665-007-9183-1

[25] Khan NA, Jamil M, Mahmood A, Ara A. Approximate solution for the electrohydrodynamic flow in a circular cylindrical conduit. ISRN Comput Math 2012.

[26] Zhou JK. Differential Transformation and Its Applications for Electrical Circuits. Huazhong Univ. Press, Wuhan, China 1986.

[27] Rashidi MM, Keimanesh M. Using differential transform method and Padé approximant for solving MHD flow in a laminar liquid film from a horizontal stretching surface. Math Prob Eng 2010; 1-14.

[28] Rashidi MM, Laraqi N, Sadri SM. A novel analytical solution of mixed convection about an inclined flat plate embedded in a porous medium using the DTM-Padé. Int J Therm Sci 2010; 49: 2405-12. http://dx.doi.org/10.1016/j.ijthermalsci.2010.07.005

[29] Rashidi MM, Laraqi N, Parsa AB. Analytical modeling of heat convection in magnetized micropolar fluid by using modified differential transform method. Heat Transf-Asian Res 2011; 40: 187-204. http://dx.doi.org/10.1002/htj.20337

[30] Rashidi MM, Keimanesh M, Bég OA, Hung TK. Magneto-hydrodynamic biorheological transport phenomena in a porous medium: A simulation of magnetic blood flow control and filtration. Int J Numer Methods Biomed Eng 2011; 27: 805-21. http://dx.doi.org/10.1002/cnm.1420

[31] Rashidi MM, Erfani E, Bég OA, Ghosh SK. Modified differential transform method (DTM) simulation of hydromagnetic multi-physical flow phenomena from a rotating disk. World J Mech 2011; 1: 217-30. http://dx.doi.org/10.4236/wjm.2011.15028

[32] Bég OA, Rashidi MM, Mehr NF. Second law analysis of hydromagnetic flow from a stretching rotating disk: DTM-Padé simulation of novel nuclear MHD propulsion systems. Frontiers Aerospace Eng 2013; 2: 29-38.

[33] Keimanesh M, Rashidi MM, Chamkha AJ, Jafari R. Study of a third grade non-Newtonian fluid flow between two parallel plates using the multi-step differential transform method. Comput Math Appl 2011; 62: 2871-91. http://dx.doi.org/10.1016/j.camwa.2011.07.054

[34] Bég OA, Rashidi MM, Keimanesh M, Bég TA. Semi-numerical modelling of "chemically-frozen" combusting buoyancy-driven boundary layer flow along an inclined surface. Int J Appl Math Mech 2013; 9: 1-1613.

[35] Parsa AB, Bég OA, Rashidi MM, Sadri SM. Semi-computational simulation of magneto-hemodynamic flow in a semi-porous channel using optimal homotopy and differential transform methods. Comput Biol Med 2013; 5: 19.

[36] Rashidi MM, Ferdows M, Uddin MJ, Bég OA, Rahimzadeh N. Group theory and differential transform analysis of mixed convective heat and mass transfer from a horizontal surface with chemical reaction effects. Chem Eng Commun 2012; 199: 1012-43. http://dx.doi.org/10.1080/00986445.2011.636850

[37] Bég TA, Rashidi MM, Bég OA, Rahimzadeh N. Differential transform semi-numerical simulation of biofluid-particle suspension flow and heat transfer in non-Darcian porous media. Comput Methods Biomech Biomed Eng 2012; DOI. ORG/ 10. 1080/10255842. 2011.643470

[38] Bég OA, Rashidi MM, Aziz A, Keimanesh M. Differential transform study of hypersonic laminar boundary layer flow and heat transfer over slender axisymmetric bodies of revolution. Int J Appl Math Mech 2012; 8: 83-108.

[39] McKee S, Watson R, Cuminato J, Caldwell J, Chen MS. Calculation of electrohydrodynamic flow in a circular cylindrical conduit. Z Angew Math Mech 1997; 77: 457-65. http://dx.doi.org/10.1002/zamm.19970770612

[40] Seyed-Yagoobi J, Bryan JE, Castaneda JA. Theoretical analysis of ion-drag pump. IEEE Trans Ind Appl 1995; 31: 469-76. http://dx.doi.org/10.1109/28.382105

[41] Chang J-S, Tsubone H, Harvel GD, Urashima K. Narrow-flow-channel-driven EHD gas pumps for an advanced thermal management of microelectronics. IEEE Trans Ind Appl 2010; 46: 1151-8. http://dx.doi.org/10.1109/TIA.2010.2045326

[42] Rada M, Darabi J, Ohadi MM, Lawler J. Electrohydrodynamic pumping of liquid nitrogen using a mesoscale ion-drag pump. IECEC 01 Energy Technologies Beyond Traditional Boundaries, Savannah, Georgia, USA 2001.

[43] Bég OA, Hameed M, Bég TA. Chebyschev spectral collocation simulation of nonlinear boundary value problems in electrohydrodynamics. Int J Comput Methods Eng Sci Mech 2013; 14: 104-15. http://dx.doi.org/10.1080/15502287.2012.698707

[44] Bég OA, Bhargava R, Rashidi MM. Numerical Simulation in Micropolar Fluid Dynamics: Mathematical Modelling of Nonlinear Flows of Micropolar Fluids. Lambert Academic Publishing, Germany 2011; p. 288, ISBN: 978-3-8454-0916-0.

[45] Baker GA, Graves-Morris P. Padé Approximants, Encyclopedia of Mathematics and Its Applications, Parts I and II, Addison-Wesley Publishing Company, New York 1981.

[46] Baker GA. Essential of Padé Approximants, Academic Press, London 1975.

[47] Rashidi MM. The modified Differential Transform Method for solving MHD boundary-layer equations. Comput Phys Commun 2009; 180: 2210-7. http://dx.doi.org/10.1016/j.cpc.2009.06.029

[48] Bég OA. Numerical methods for multi-physical magnetohydrodynamics, Chapter 1, pp. 1-110, New Developments in Hydrodynamics Research, Nova Science, USA 2012.

[49] Gorla RSR, Gatica JE, Ghorashi B, Ineure P, Bird LW. Heat transfer in a thin liquid film in the presence of an electric field. Chem Eng Commun 2004; 191: 718-31. http://dx.doi.org/10.1080/00986440490276038

Received on 03-10-2013 Accepted on 30-10-2013 Published on 10-02-2014

DOI: http://dx.doi.org/10.12970/2311-1755.2013.01.02.3